

NEW 2MASS NEAR-INFRARED PHOTOMETRY FOR GLOBULAR CLUSTERS IN M31

SONG WANG^{1,2}, JUN MA¹, ZHENYU WU¹, AND XU ZHOU¹

Draft version April 18, 2014

ABSTRACT

We present 2MASS JHK_s photometry for 913 star clusters and candidates in the field of M31, which are selected from the latest Revised Bologna Catalog of M31 globular clusters (GCs) and candidates. The photometric measurements in this paper supplement this catalog, and provide a most comprehensive and homogeneous photometric catalog for M31 GCs in the JHK_s bandpasses. In general, our photometry is consistent with previous measurements. The globular cluster luminosity function (GCLF) peaks for the confirmed GCs derived by fitting a t_5 distribution using maximum likelihood method are: $J_0 = 15.348^{+0.206}_{-0.208}$, $H_0 = 14.703^{+0.176}_{-0.180}$, and $K_{s0} = 14.534^{+0.142}_{-0.146}$, all of which agree well with previous studies. The GCLFs are different between metal-rich (MR) and metal-poor (MP), inner and outer subpopulations, as that MP clusters are fainter than their MR counterparts, and the inner clusters are brighter than the outer ones, which confirm previous results. The NIR colors of the GC candidates are on average redder than those of the confirmed GCs, which lead to an obscure bimodal distribution of the color indices. The relation of $(V - K_s)_0$ and metallicity shows a notable departure from linearity, with a shallower slope towards the redder end. The color-magnitude diagram (CMD) and color-color diagram show that many GC candidates are located out of the evolutionary tracks, suggesting that some of them may be false M31 GC candidates. The CMD also shows that the initial mass function of M31 GCs covers a large range, and the majority of the clusters have initial masses between 10^3 and $10^6 M_\odot$.

Subject headings: catalogs – galaxies: individual (M31) – galaxies: spiral – galaxies: star clusters: general

1. INTRODUCTION

Globular clusters (GCs) provide a unique laboratory for investigating the formation and evolution of their host galaxies. The form of the mass spectrum for GCs is nearly identical to the mass function of the parent molecular cloud cores (McLaughlin & Pudritz 1996). The brightness distribution of GCs, known as globular cluster luminosity function (GCLF), can be used to constrain possibilities for GC formation and destruction (see Nantais et al. 2006, and references therein).

By virtue of the natural advantage of being located at a reasonable distance, nearby galaxies (especially M31) offer us an ideal environment for detailed studies of cluster systems. A large number of GCs have been identified in M31 since Hubble (1932), and the latest Revised Bologna Catalog of M31 GCs and candidates (hereafter RBC V.5, Galleti et al. 2004, 2006, 2009), which is a compilation of photometry and identifications from many previous catalogs, published 625 confirmed GCs and 331 GC candidates. Based on the growing number and updated sample of M31 GCs and candidates, many works have probe the GCLF in M31 in detail. Crampton et al. (1985) found that the mean luminosity of GCs in M31 decreases markedly with increasing galactocentric distance, indicating that clusters with larger projected distances are fainter than those closer to the nucleus (Gnedin 1997). Ostriker & Gnedin (1997) obtained distance moduli to M31 and M87 from GCLF by applying the corrections for dynamical evolution, and found surprising consistency of the predicted and observed distances, which confirmed the GCLF as a distance indicator. These authors also concluded that the mass functions of GCs in the Milky Way (MW), M31, and M87 were universal at the birth of these systems, although

spanning a wide range of masses. Barmby et al. (2001) measured the LF for M31 GCs, and found that inner clusters have a GCLF peak brighter than the outer ones, while the metal-rich (MR) clusters are brighter than their metal-poor (MP) counterparts. The variation in the M31 GCLF seems to be due to various factors: metallicity, age, cluster initial mass function (IMF), and dynamical destruction (Barmby et al. 2001). Recently, Nantais et al. (2006) compared the GCLFs of the MW, M31, and the Sculptor Group spiral galaxies, and found that the GCLF of the MW is consistent with that of M31.

Near-infrared (NIR) colors can help to distinguish among star formation histories and IMFs (Barton Gillespie et al. 2003). The Two Micron All Sky Survey (2MASS), performed between 1997 June and 2001 February, covers 99.998% of the celestial sphere in the J ($1.25 \mu\text{m}$), H ($1.65 \mu\text{m}$), and K_s ($2.16 \mu\text{m}$) bandpasses (Skrutskie et al. 2006). These observations were conducted with two 1.3 m diameter telescopes located at Arizona and Chile. The 2MASS All-Sky Data Release contains the observation of M31 with an integration time of 7.8 s for each exposure, while a new 2.8 deg^2 NIR survey from the 2MASS 6X program across the extent of the optical disk of M31, with an exposure time of 6 times the normal exposure, provides a clearer view of the galaxy center. Galleti et al. (2004) identified 693 known and candidate GCs in M31 using the 2MASS database, and derived their 2MASS JHK_s magnitudes. After adding the mean difference between the 2MASS photometry and previous NIR photometry, the newly assembled NIR dataset were implemented into a revised version of Bologna Catalog. These authors also showed that the $V - K_s$ color provides a powerful tool to discriminate between M31 clusters and background galaxies. Santos et al. (2013) presented 2MASS photometry and color for a sample of Local Group clusters younger than ~ 100 Myr, and found that the embedded clusters, which are heavily obscured by dust, generally have a redder $H - K_s$ color than older ones, from which gas and dust have already been ejected. These authors also

¹ Key Laboratory of Optical Astronomy, National Astronomical Observatories, Chinese Academy of Sciences, Beijing 100012, China; majun@nao.cas.cn

² University of Chinese Academy of Sciences, Beijing 100039, China

concluded that the brightest clusters can be split into young and old subsamples from $H - K_s$ color. Considering that a more extended and homogenous photometry in the NIR is important for the studies on M31 star clusters, we would carry out new photometry for them using 2MASS images.

In this paper, we provide NIR photometry for a set of star clusters in M31 using images from 2MASS. This paper is organized as follows. In Section 2 we present the sample selection, JHK_s photometry, and comparisons with previous measurements. A discussion on the properties of the sample clusters will be given in Section 3, including the GCLF and color distributions. Finally, we will summarize our results in Section 4.

2. DATA

2.1. Sample

We selected our sample GCs and candidates from RBC V.5, which contains precise cluster coordinates, classifications, metallicities, reddening values, radial velocities, galactocentric distances, structure parameters, and photometry including *GALEX* (FUV and NUV), optical broad-band, and 2MASS NIR magnitudes for 2060 objects. However, RBC V.5 provided JHK_s magnitudes in three bands only for ~ 1100 objects. In addition, there were no magnitude errors for JHK_s bands in RBC V.5. Therefore, homogeneous photometric data and precise magnitude errors for JHK_s bands are urgently needed. We selected classes 1, 2, 3, and 8 from column ‘f’ in RBC V.5, which include GCs, candidate GCs, controversial objects, and extended clusters. This resulted in an initial selection of 991 objects. We first employed IRAF/DAOFIND to find the sources in the images and matched them to the coordinates of these objects given by RBC V.5, and then checked each object visually in the images to confirm the positions for the photometry. During this process, we found that there are 68 clusters for which accurate photometric measurements cannot be obtained with different reasons. Some clusters (B024D, B053D, B061D, B523, B537, BH16, M023, SK068B, SK110A) are superimposed onto a bright or strongly variable background. Some clusters (B102D, HEC2, MCEC4) are very faint and the signal-to-noise ratio (S/N) is low. Some clusters (B189D, B246, B274, B538, BH09, BH25, C011, C041, KHM31-77, M050, M065, M075, M078, NB89, SK059B, SK061A, SK063C, SK097B, SK104B, SK153C) are very close to other objects. Some clusters (B016D, B088D, B530, BH01, BH03, BH04, BH28, DAO93, H20, HEC6, HEC9, HEC13, KHM31-345, M055, M079, NB17, SH06, SK049A, SK222C, SK216B, SK223B, SK242B) are indiscernible with the coordinates presented by RBC V.5 in the 2MASS images. There is one or two nearby objects within 2–4 pixels for five clusters (B016D, B530, M055, SH06, SK223B) of them, however, after careful comparison with the images from Local Group Survey (LGS; Massey et al. 2006) and from Digitized Sky Survey (DSS), these objects cannot be confirmed due to their low S/N values. In addition, we found that some clusters (B196D, B257D, B318, B368, B453, B475, G099, KHM31-85, M056, M068, M088, M089, SK166B, V031) have one or more nearby bright objects in the images from LGS or from Wide Field Planetary Camera on *Hubble Space Telescope*, indicating that they are “adhered” in 2MASS images because of the poor resolution. Ma (2012b) presented JHK_s photometry, ages, and masses for 10 newly-discovered halo GCs in M31. So, we will not re-estimated JHK_s magnitudes for these GCs. Fi-

nally, here we will derive NIR photometry for the remaining 913 star clusters and cluster candidates. The position of cluster H26 presented by RBC V.5 may be of insufficient accuracy, with R.A. and decl. being 00:59:27.37 and +37:41:34.1 (Huxor et al. 2008). We checked the images from 2MASS and from DSS, and corrected the coordinate to 00:59:27.48 and +37:41:31.37. The updated position was then used for the following photometry. Figure 1 shows the spatial distribution of the sample clusters in M31.

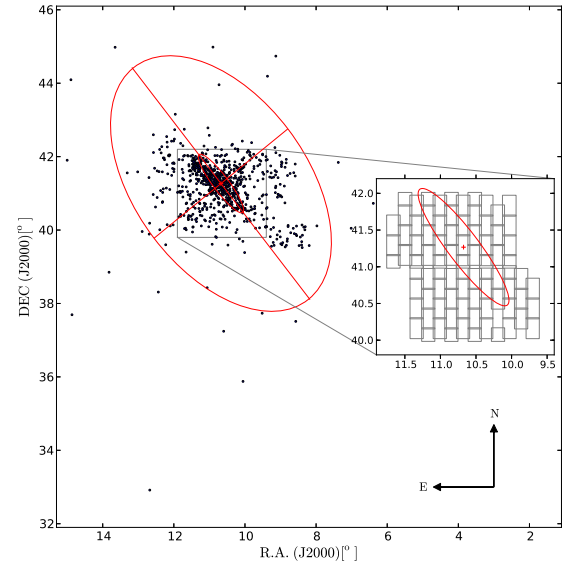


FIG. 1.— Location of our sample star clusters in relation to M31. The inner red ellipse has a radius of $R = 1^\circ$ and an inclination angle of $i = 77.5^\circ$, while the outer red ellipse has a radius of 55 kpc and is flattened to $b/a = 0.6$, as given in Richardson et al. (2009). The filled circles represent the sample clusters in this paper. The subplot presents the used images from 2MASS-6X survey, and the red ellipse has the same dimension of $R = 1^\circ$.

2.2. Integrated Photometry

We used the 2MASS archival images of M31 in the JHK_s bands to do photometry. The images were retrieved using the 2MASS Batch Image Service³. Considering that the 2MASS-6X images, which were observed with 6 times the normal exposure of 7.8 s, have a deeper magnitude limit and a higher S/N than the All-Sky Release Survey images, the 2MASS-6X data were preferred. In this paper, photometry for 627 objects were performed using the 2MASS-6X data, while photometry for the rest 286 ones were done using the All-Sky Release Survey data. The uncompressed atlas images provided were used, with a resampled spatial resolution of $\sim 1'' \text{ pixel}^{-1}$. We performed aperture photometry of the 913 M31 star clusters in all of the JHK_s bands to provide a comprehensive and homogeneous photometric catalog for them. The photometry routine we used is IRAF/DAOPHOT (Stetson 1987).

To determine the total luminosity of each object, we produced a curve of growth from J -band photometry obtained through apertures with radii in the range of 4–16 pixel with 1 pixel increments. The most appropriate photometric radius from the curve that encloses the total cluster light but excludes

³ <http://irsa.ipac.caltech.edu/applications/2MASS/IM/batch.html>.

lights from extraneous field stars were adopted. In addition, we checked the images of all the three bands for each cluster by visual examination to make sure that the photometric aperture was not so large as to be contaminated by other sources. The local sky background was measured in an annulus with an inner radius 1 pixel larger than the photometric radius and 5 pixels wide. The sky fitting algorithm was set to “mode”. The derived magnitudes with large uncertainties (> 1 mag) were abandoned here to keep high photometry precision. The instrumental magnitudes were then calibrated using the relevant zero points obtained from the photometric header keywords of each image. Figure 2 shows the aperture distribution as a function of J -band magnitude, with a highest peak at $4''$. In general, magnitudes of brighter objects are measured with larger apertures.

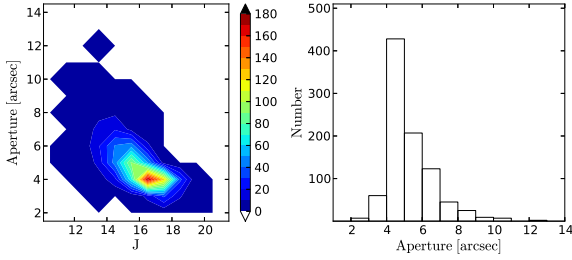


FIG. 2.— (Left panel) Contour plot of the aperture as a function of J -band magnitude. (Right panel) Aperture distribution for M31 star clusters.

Finally, except for 9 objects in the J band, 31 objects in the H band, and 51 objects in the K_s band, we obtained photometry for 913 star clusters in the individual JHK_s bands. Table 1 lists our new JHK_s magnitudes and the aperture radii used, in conjunction with the magnitude uncertainties given by DAOPHOT. Figure 3 shows the uncertainty distribution as a function of magnitude for the JHK_s bands. Filled circles represent photometry performed on the 2MASS-6X images, while red pluses represent photometry performed on the 2MASS All-Sky images. It is clear that the photometry from 2MASS-6X data show smaller magnitude uncertainties, which are due to high S/N with longer exposures. Objects in these dashed boxes are bright sources with slightly large magnitude uncertainties (> 0.2 mag). Six clusters (AU008, AU010, B132, NB21, NB39, NB41) have large magnitude uncertainties in all three bands, two clusters (B070, B119) have large magnitude uncertainties in K_s band, two clusters (B104, NB108) have large magnitude uncertainties in JH bands, and three clusters (B264, B324, SK050A) have large magnitude uncertainties in HK_s bands. All these clusters are close to the galaxy center and suffer from a bright background contamination.

2.3. Comparison with Previously Published Photometry

To examine the quality and reliability of our photometry, we compared the aperture magnitudes of the 913 objects obtained here with previous results, in the sense of values from this paper minus values from the others. Figure 4 and Figure 5 plot the comparison of our obtained 2MASS photometry with the aperture photometry from 2MASS catalog, with $r = 4''$ for the Point Source Catalog (PSC) and $r = 5''$ for the Extended Source Catalog (XSC) following Galleti et al. (2004). The 2MASS PSC was derived by combining the 2MASS All-

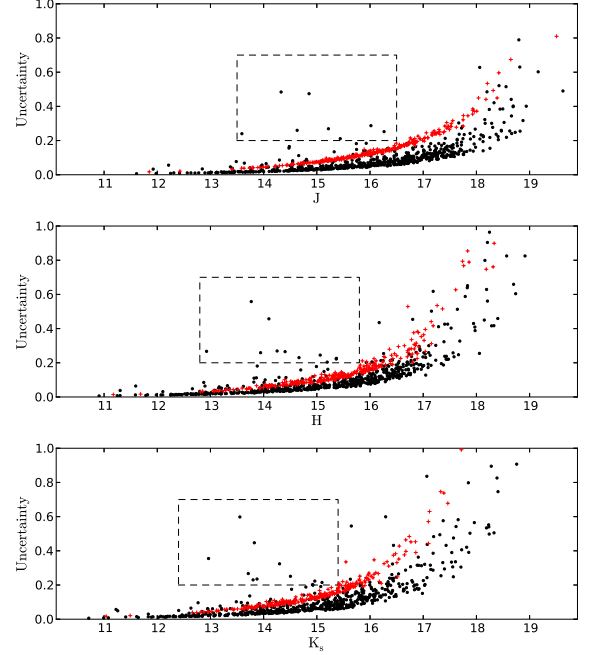


FIG. 3.— Distribution of uncertainty as a function of magnitude for the JHK_s bands. The filled circles represent photometry performed on the 2MASS-6X images, while the red pluses represent photometry measured on the 2MASS All-Sky images. Objects in these dashed boxes are bright sources with slightly large magnitude uncertainties.

Sky PSC and the 2MASS 6X Point Source Working Database (6X-PSWDB), with the 6X-PSWDB being preferred. The 2MASS XSC was derived by combining the 2MASS All-Sky XSC and the 2MASS 6X Extended Source Working Database (6X-XSWDB), with the 6X-XSWDB being preferred. Each panel displays the mean difference (Δ), rms scatter (σ), and the number points (N) for the comparison. There were nine objects with larger offset ($|\Delta m| > 1$ mag) for the comparison with PSC, as listed in Table 2. It was surprised that the magnitudes of eight of these clusters were measured with an aperture of $r = 4''$ here, which is the same as adopted in the PSC. We checked the images for these clusters and found that some clusters (SK049C, SK054C, SK086C) are located in a strongly variable background, while some clusters (B038D, B104, SK047B) lie close to the M31 center. In addition, there is one very bright source near SK115B. For objects in the PSC, the sky background is measured in an annulus with an inner radius of $14''$ and an outer radius of $20''$. To check whether the discrepancy is caused by the different choice of the annulus for background, we used the same annulus with PSC and re-estimated magnitudes for the eight clusters. We found that most of the newly derived magnitudes agree well with those from PSC, except SK115B, and SK136C. For SK115B, about a quarter of the area of the annulus ($14''$ - $20''$) is affected by the nearby bright source, which would lead to a high estimate of the sky background. For SK136C, the J -band magnitude given by PSC is 13.419, much brighter than the H -band magnitude 16.700, which is suspicious. We think that the annulus set in this paper is more reasonable for these clusters. In addition, for cluster B072D, a larger radius would include lights from outer sources. In this paper, photometry was performed with an aperture radius larger than $4''$ for more than 400 clusters, which may lead to brighter magnitudes than

those in 2MASS PSC, on the average. We concluded that this is the main reason for the offset of the JHK_s magnitudes (-0.029 , -0.051 , and -0.060). There is no big difference between the magnitudes measured here and those from the XSC.

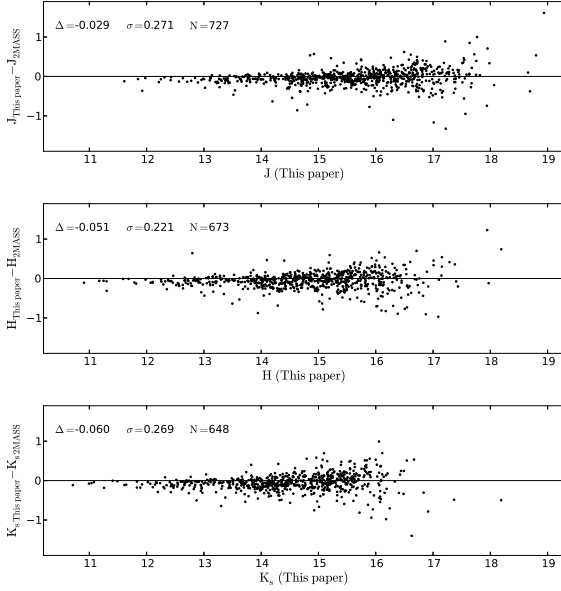


FIG. 4.— Comparison of our obtained 2MASS photometry with previous measurements from 2MASS PSC. The Δ , σ , and N represent the mean difference, rms scatter, and the number points used for the comparison, respectively.

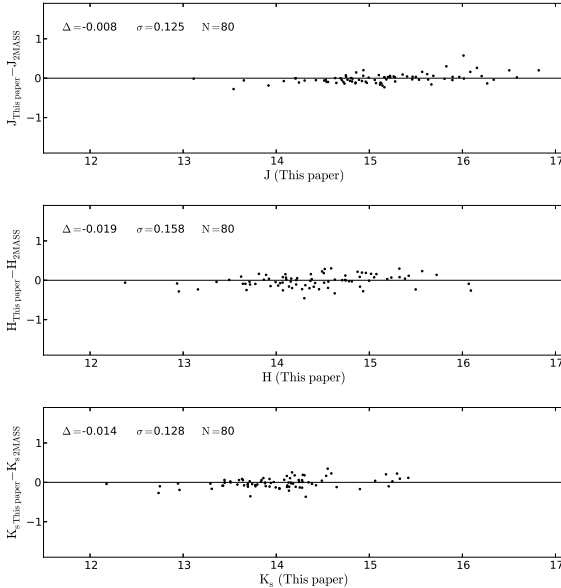


FIG. 5.— Comparison of our obtained 2MASS photometry with previous measurements from 2MASS XSC. The numbers are as in Fig. 4.

Barmby et al. (2000) measured JK magnitudes for a sample of M31 GCs, with most of the new NIR data taken with the STELIRCam on the 1.2 m telescope at Fred Lawrence

Whipple Observatory (FLWO), and the observation data for four objects from the 2MASS (Skrutskie et al. 1997) scans of M31. Barmby et al. (2001) obtained NIR photometry for 38 GCs and candidates from JHK' observation using the Gemini on the Lick Observatory 3 m telescope and JK observation using the STELIRCam on the FLWO 1.2 m, and updated magnitudes for some clusters studied in Barmby et al. (2000). Figure 6 plots the comparison of our obtained 2MASS photometry with the magnitudes from Barmby et al. (2000, 2001). The average differences for the J and K_s bands are 0.024 and -0.032 , which may be caused by different photometry methods, with the rms scatters around the mean being 0.193 and 0.231. There is only one cluster (DAO69) with larger magnitude offsets, as listed in Table 2. A larger radius would include lights from several outer sources, so we think our photometry result is more reasonable for DAO69.

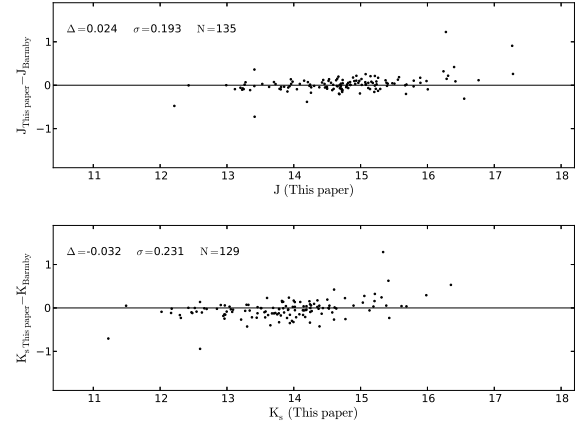


FIG. 6.— Comparison of our obtained 2MASS photometry with previous NIR measurements from Barmby et al. (2000, 2001). The numbers are as in Fig. 4.

Figure 7 displays the comparison of our obtained 2MASS photometry with the magnitudes from RBC V.5. The 2MASS photometry in RBC V.5 (Galleti et al. 2004) was derived from the 2MASS All-Sky PSC and XSC, by correcting the systematic shifts between the magnitudes from the 2MASS catalogs and previous NIR photometries. In RBC V.5, the 2MASS JHK_s magnitudes were transformed to CIT photometric system (Galleti et al. 2004). However, we needed the original 2MASS JHK_s data to compare with our results, so we reversed the transformation using the equations given by Carpenter (2001). The average differences for the three bands are 0.059, 0.050 and 0.032, with the rms scatters around the mean being 0.309, 0.264 and 0.327. There is an obvious offset between their estimated J magnitudes and ours, which is mainly caused by some large scatters listed in Table 2. If these clusters with larger offset ($|\Delta m| > 1$ mag) are not included, the systematic offset in J band can be reduced to be 0.035 mag. The clusters with the largest discrepancy are B041, B090, and SK054C. There are several bright sources beyond B041, and a larger radius would include lights from these sources. The K_s magnitude of B090 in RBC V.5 is 17.881, which is from the 2MASS All-Sky PSC. However, in the 2MASS 6X-PSWDB, the magnitude is 15.308. We checked the images of the 2MASS All-Sky survey, and found that the low S/N is the main reason for the K_s magnitude inaccuracy.

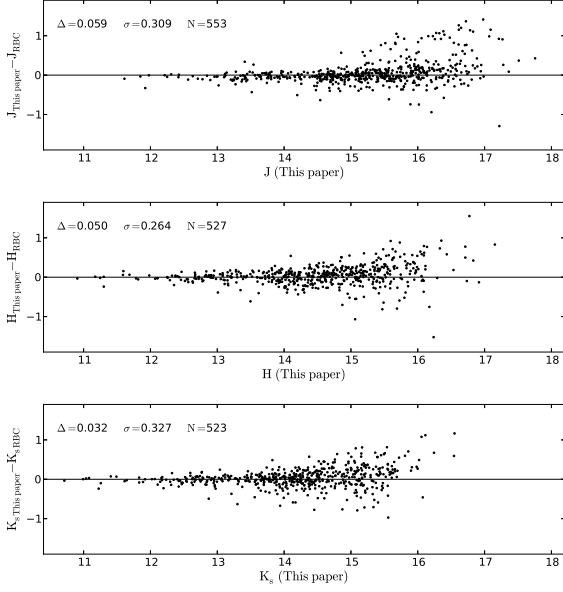


FIG. 7.— Comparison of our obtained 2MASS photometry with previous NIR measurements from RBC V.5. The numbers are as in Fig. 4.

The four objects with magnitude scatters larger than 2.0 mag are plotted in Figure 8, in which the circles are photometric apertures adopted here. As discussed above, the inaccuracy of the K_s photometry for B090 is mainly caused by the low S/N. B104 lies close to the M31 center, while SK054C is located in a variable background. The different annulus set for the sky estimation results in the discrepancy of the magnitudes, and we think that the photometry method in this paper is more reasonable for these clusters. For SK136C, the J magnitude in 2MASS PSC (13.419), which is much brighter than H magnitude (16.700), may be a typing error. In all comparisons the average absolute difference is ≤ 0.06 mag, and the rms scatter around the mean varies between 0.1 and 0.4. No system offset between our magnitudes and previous determinations can be seen.

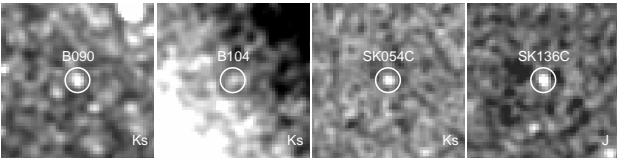


FIG. 8.— Images of four star clusters, of which the magnitude scatters between this paper and other previous studies are larger than 2.0 mag. The circles are photometric apertures adopted in this paper.

2.4. Extinction Correction and Metallicity

Caldwell et al. (2009, 2011) published reddening values for a large sample of clusters in M31 by comparing the observed spectra with model ones. Considering the high accuracy of their spectral results, we preferentially adopted Caldwell et al. (2009, 2011) reddening values. However, the mode value of 0.13 and values from Barmby et al. (2000) in Caldwell et al. (2009, 2011) were not adopted. For star clusters with no reddening value given by Caldwell et al. (2009, 2011), we adopted the results from Barmby et al. (2000),

Fan et al. (2008), and Fan et al. (2010). Barmby et al. (2000) and Fan et al. (2008) determined the reddening for M31 clusters using correlations between optical and infrared colors and metallicity by defining various “reddening-free” parameters. Because the reddening values from Fan et al. (2008) comprise a homogeneous data set and the number of GCs included is greater than that of Barmby et al. (2000), we preferentially adopted Fan et al. (2008) reddening values, followed by those of Barmby et al. (2000). Finally, the results from Fan et al. (2010), which derived reddening values from spectral-energy distribution fitting, were adopted.

There are 378 star clusters with no available reddening values in the literatures, and we would calculate reddening values for them in a similar way as described in Kang et al. (2012). For clusters with a de-projected galactocentric distance < 22 kpc, the reddening values were measured as the mean reddening values of star clusters located within an annulus at every 2 kpc radius from the center of M31. While for clusters beyond a de-projected distance of 22 kpc, most of which are located in halo regions, the reddening value of $E(B - V) = 0.13$ mag was adopted as Kang et al. (2012) suggested.

Caldwell et al. (2011) provided new homogeneous estimates of metallicity for more than 300 GCs in M31, using high-quality spectra obtained with the Hectospec multifiber spectrograph on the 6.5 m MMT. Kang et al. (2012) derived mean value of metallicities for a catalog of clusters from previous literatures (Barmby et al. 2000; Perrett et al. 2002; Galleti et al. 2009; Caldwell et al. 2011). Metallicities for 312 and 289 clusters in our sample were given by Caldwell et al. (2011) and Kang et al. (2012), respectively. Table 1 lists the metallicities from Caldwell et al. (2011) and Kang et al. (2012) for the sample clusters.

3. DISCUSSION

We combined the photometry results of JHK_s bands newly derived here with those derived by Ma (2012b) for 10 GCs in the M31 halo to construct a more comprehensive sample of 923 clusters in M31 to discuss the properties for them. The reddening values for the 10 GCs were derived from Ma (2012b), while the metallicities from Caldwell et al. (2011) and Kang et al. (2012) were used for them, respectively. The V -band magnitudes of the sample clusters were derived from RBC V.5 for the following analysis about the color distribution. All these magnitudes have been extinction corrected.

3.1. Luminosity Function

To obtain the M31 GCLF peaks, we used least square and maximum likelihood methods to fit a Gaussian and Student’s t distribution on the dereddened JHK_s data. The Gaussian distribution is given as

$$f(x) = \frac{1}{\sqrt{2\pi}\sigma_G} \exp\left(-\frac{(x - \mu_G)^2}{2\sigma_G^2}\right) \quad (1)$$

The Student’s t distribution is defined by

$$f(x) = \frac{\Gamma((n+1)/2)}{\sqrt{\pi} n \Gamma(n/2) \sigma_t} \left(1 + \frac{(x - \mu_t)^2}{n\sigma_t^2}\right)^{-(n+1)/2} \quad (2)$$

where n is the degree of freedom (DOF). Secker (1992) and Secker & Harris (1993) reported that the Student’s t distribution with DOF of 5 (hereafter “ t_5 ”), which presents a power-law fall-off in its wings, is more robust than the Gaussian in describing the outlying data points and estimating the GCLF

peak. The “ t_5 ” function is evaluated as

$$f(x) = \frac{8}{3\sqrt{5}\pi\sigma_t} \left(1 + \frac{(x - \mu_t)^2}{5\sigma_t^2}\right)^{-3} \quad (3)$$

Some other distributions (Baum et al. 1995; Larsen et al. 2001) were also investigated for the GCLF. Baum et al. (1995) found that a composite of two exponentials is a better fit over the Gaussian or Student’s t distribution to the combined LF of the Galactic and M31 GCs, since those two distributions fail to deal with the asymmetry and with the sharpness of the peak of the histogram.

Figure 9 displays the luminosity histograms and the best fitting lines for the sample clusters. The top panels show the fitting with least square technique, while the bottom panels show the fitting with maximum likelihood method. The black lines show the fitting with a t_5 distribution, while the red lines show the fitting with a Gaussian distribution. The maximum likelihood method is used to estimate the most probable parameter values from the sample data (Secker 1992), which would not suffer from the effect of binning. As shown in Figure 9, the fitting with a t_5 distribution shows a more extended wing than that with a Gaussian distribution (Secker 1992). Table 3 lists the LF parameters for the sample clusters, the confirmed GCs, and those confirmed GCs with metallicities available from Kang et al. (2012). The LF peaks for confirmed GCs are much brighter than those for all clusters, indicating that a clean sample of GCs is critical to obtain accurate LF parameters.

The GCLF peaks derived by Barmby et al. (2001) are $J_0 = 15.26$ and $K_0 = 14.45$, by fitting a t_5 distribution using the MAXIMUM program written by J. Secker (see Secker 1992, for details). Nantais et al. (2006) derived similar results for the JHK_s bands using same methods: $J_0 = 15.31$, $H_0 = 14.76$, and $K_{s0} = 14.51$, and these authors concluded that the little fainter peaks than those from Barmby et al. (2001) could be real, due to a larger and possibly deeper sample. In this paper, the LF peaks for the confirmed GCs, derived by fitting a t_5 distribution using maximum likelihood method, are: $J_0 = 15.348^{+0.206}_{-0.208}$, $H_0 = 14.703^{+0.176}_{-0.180}$, and $K_{s0} = 14.534^{+0.142}_{-0.146}$, all of which agree well with previous results. The σ parameters derived here are slightly larger than previous studies.

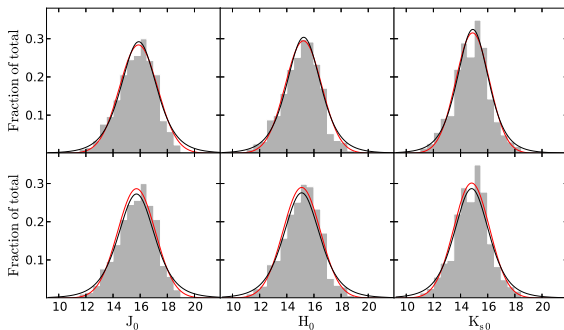


Fig. 9.— The luminosity histograms and the best fitting models for the sample clusters. The top panels show the fitting with least square technique, while the bottom panels show the fitting with maximum likelihood method. The black and red lines show the fitting with a t_5 and Gaussian distribution, respectively.

It has long been known that the peak of the GCLF is nearly constant in different galaxies, providing a standard indica-

tor for the cosmological distance measurement (Racine 1968; Hanes 1977; Ferrarese et al. 2000). However, several studies (Crampton et al. 1985; Gnedin 1997; Barmby et al. 2001) presented that GCLF varies between MR and MP, inner and outer subsamples within a galaxy, and GCLF peak becomes fainter as the local density of galaxies increases (Blakeslee & Tonry 1996). Larsen et al. (2001) found that the V -band turnover of the blue GCs is brighter than that of the red ones by about 0.3 mag on the average, with a study of GCs in 17 nearby early-type galaxies. Barmby et al. (2001) found that MR clusters are brighter than MP ones in M31, and inner clusters are brighter on average than outer clusters, indicating that the luminosity function is different among these subpopulations. Goudfrooij et al. (2004) confirmed that the GC system in the early-type galaxy NGC 1316, which is an intermediate-age merger remnant, can be divided into a blue GC subpopulation, consistent with a Gaussian LF, and a red GC component with a power law LF. These authors also found that the LF of the inner half of the MR population differs significantly from that of the outer half. The difference in GCLF between dwarf and giant ellipticals has been studied by many authors (Harris 1991; Durrell et al. 1996; Strader et al. 2006; Jordán et al. 2006; Miller & Lotz 2007), however, whether there is a trend of the GCLF peak with the galaxy luminosity is still under debate.

To investigate the effects of metallicity and galactocentric distance on the LF, we divided the confirmed GCs into four subsamples as Barmby et al. (2001) did. The MR and MP subpopulations are divided at $[\text{Fe}/\text{H}] = -1.1$, using metallicities from Kang et al. (2012), while the inner and outer subsamples are divided at $R_{\text{gc}} = 10$ kpc. Figure 10 displays the J_0 luminosity histograms for the four subsamples, together with the best-fit t_5 distribution using the maximum likelihood method. Table 4 lists the GCLF fit results in the JHK_s bands for the four subsamples. It is evident that the MP clusters are fainter than their MR counterparts, and the inner clusters are brighter than the outer ones. Gnedin (1997) reported that the destruction of the inner faint, low-density clusters due to strong tidal shocks may lead to the difference between the LF of the inner and outer populations. Kavelaars & Hanes (1997) asserted that the difference in the GCLF of the inner and outer halo populations is due to dynamical evolution and/or a dependence of GCLF shape on the environment. Ostriker & Gnedin (1997) found that the predicted differences between the peaks of the inner and outer cluster populations, due to the tidal shocks and dynamical friction, agree quantitatively with the observed differences within the errors in the MW, M31, and M87. However, Barmby et al. (2001) concluded that metallicity, age, and cluster IMF may also be important for the variation in the M31 GCLF except dynamical destruction.

3.2. Color Distribution

Figure 11 displays the NIR color (including $(V - K_s)_0$) distribution of the whole sample clusters (solid-line histogram) and the confirmed GCs (filled histogram) with magnitude uncertainty < 0.5 mag. There are some bumps located in the redder wings of the $(J - K_s)_0$, $(H - K_s)_0$, and $(V - K_s)_0$ colors, which are mainly caused by GC candidates. The GC systems of many galaxies reveal bimodal optical color distributions (Forbes et al. 1997; Kundu et al. 1999; Gebhardt & Kissler-Patig 1999; Larsen et al. 2001; Rejkuba 2001). Barmby et al. (2000) have detected the bimodal distribution of the GC colors in M31 using $(U - V)_0$, $(U - R)_0$,

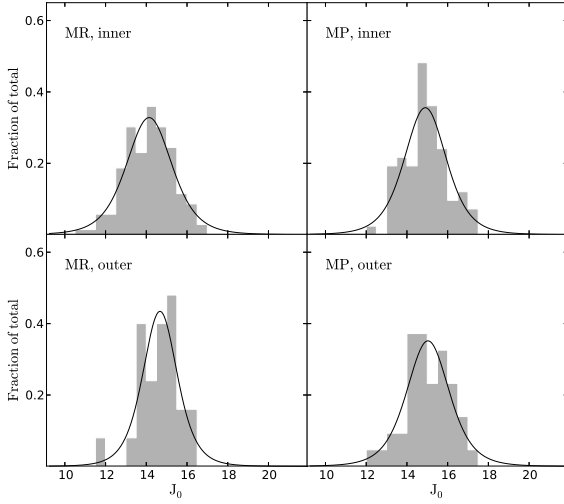


FIG. 10.— The J_0 luminosity histograms and the best fitting models for four groups of the confirmed GCs, divided by the galactocentric distances and metallicities from Kang et al. (2012). The black lines show the fitting with a t_5 distribution using the maximum likelihood method.

and $(V - K)_0$ with the KMM statistics (McLachlan & Basford 1988; Ashman et al. 1994). To check whether the NIR color distributions are bimodal, the KMM algorithm was also performed here. The homoscedastic fitting, with same variances for both groups, was assumed. Table 5 lists the parameters returned by the KMM algorithm. Column (2) and (3) give the estimated mean value and covariance assuming the whole sample as one group. Column (4) and (5) give the estimated mean value for each group, assuming the whole sample as two groups, and Column (6) gives the common covariance for them. Column (7) and (8) give the number points assigned to each group. Column (9) gives the p value, which is an estimate of the improvement of the two-group fit over a one-group fit, and is interpreted as a rejection of the single Gaussian model at a confidence level of $1 - p$. The purely NIR color distributions show bimodality at the ~ 100 per cent confidence level, however, the size of the redder subsample is very small, and this subsample is composed mainly of the GC candidates, as shown in Figure 11. Although Table 5 presents the mean values and number points for the two groups of $(V - K_s)_0$ color, these values vary with the initial set, and the p value is unavailable since the sample is not convergent. Some previous studies of purely NIR and optical-NIR GC colors in different galaxies have shown that in some cases the optical color distributions are clearly bimodal, however, the purely NIR and optical-NIR color distributions are not, or they display “differing bimodalities” (Blakeslee et al. 2012) with those of the optical colors alone (see Cantiello et al. 2014, and references therein).

Figure 12 shows the relation between metallicity and intrinsic colors for the sample clusters with magnitude uncertainty < 0.5 mag. Metallicities in the top panels are from Kang et al. (2012), while metallicities in the bottom panels are from Caldwell et al. (2011). The open circles represent the confirmed GCs, while the crosses represent the rest clusters, including candidate GCs, controversial objects, and extended clusters. The $(V - K_s)_0$ color index, which is often used as a metallicity indicator, shows a clearer correlation with $[\text{Fe}/\text{H}]$ than other NIR colors, indicating that these NIR intrinsic

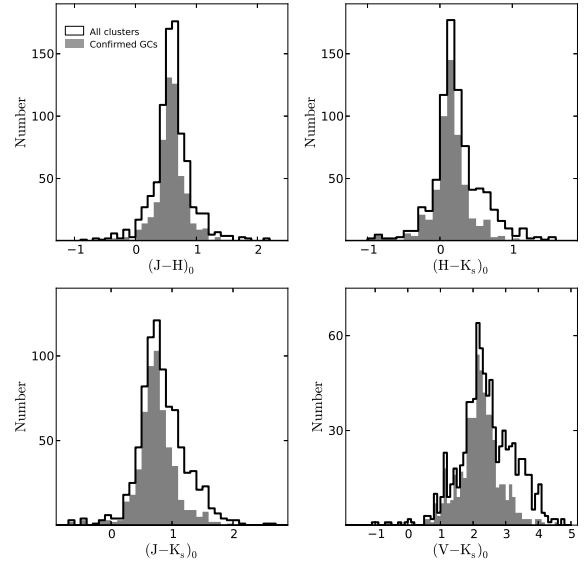


FIG. 11.— The color distribution of the sample clusters.

colors are less sensitive to metallicity (Barmby et al. 2000). Nantais et al. (2006) also reported that stellar spectra in the NIR is much less dependent on metallicity than in the optical. The relation of $(V - K_s)_0$ and metallicity shows a notable departure from linearity, with a shallower slope in the redder part. The nonlinear correlation of color with metallicity, which are mainly driven by the horizontal-branch stars, can produce a bimodal color distribution with unimodal metallicity for a group of old clusters (Yoon et al. 2006).

We also use the KMM algorithm to investigate the bimodality of the metallicity distributions for M31 GCs. Table 6 lists the parameters returned by the KMM algorithm. The average metallicities for Caldwell et al. (2011) and Kang et al. (2012) are nearly consistent, while both the two groups from Kang et al. (2012) are metal-richer than the two groups from Caldwell et al. (2011). Metallicities from Kang et al. (2012) show strong bimodal distribution at the 99.8% confidence level, while the hypothesis of a unimodal distribution is rejected only at $\sim 64\%$ confidence level for metallicities from Caldwell et al. (2011). Although many previous studies (Ashman & Bird 1993; Barmby et al. 2000; Perrett et al. 2002; Fan et al. 2008) have reported that the metallicity distribution in M31 is bimodal, Caldwell et al. (2011) suggested that the metallicity distribution in M31 is not generally bimodal, in strong distinction with the bimodal Galactic globular distribution.

Figure 13 shows the relation between intrinsic colors and galactocentric distance R_{gc} for the sample clusters. Symbols are as in Figure 12. It can be seen that the colors of candidate GCs are on average redder than those of the confirmed GCs. We derived the mean color values in different projected galactocentric distance for the confirmed GCs. For clusters with galactocentric distance $R_{\text{gc}} < 30$ kpc and $R_{\text{gc}} > 30$ kpc, the mean values were measured with star clusters located within an annulus at every 3 kpc and 10 kpc radius from the center of M31, respectively, all of which were plotted with squares in Figure 13. Crampton et al. (1985) found that no radial $(B - V)_0$ color gradient exists for M31 GCs, however, Sharov (1988) reported that the $(V - K)_0$ color shows a weak correlation with

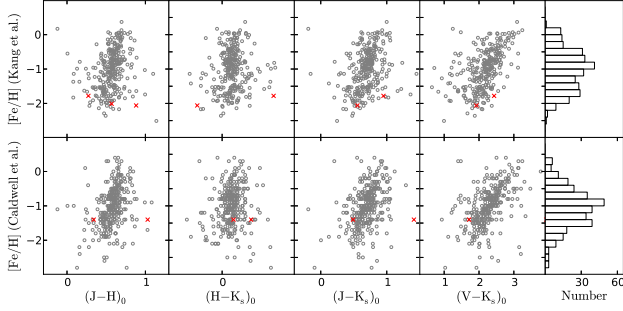


FIG. 12.— Metallicity as a function of color. The open circles represent the confirmed GCs, while the red crosses represent the rest clusters, including candidate GCs, controversial objects, and extended clusters.

the galactocentric distance. No clear trend is present between the NIR colors and R_{gc} for the confirmed GCs. It seems that clusters with R_{gc} around 20 kpc are on average redder than inner clusters in the $(V - K_s)_0$ color index, however, this may be caused by the crowding blue clusters around the “10 kpc ring” (Gordon et al. 2006), which pull the color index down.

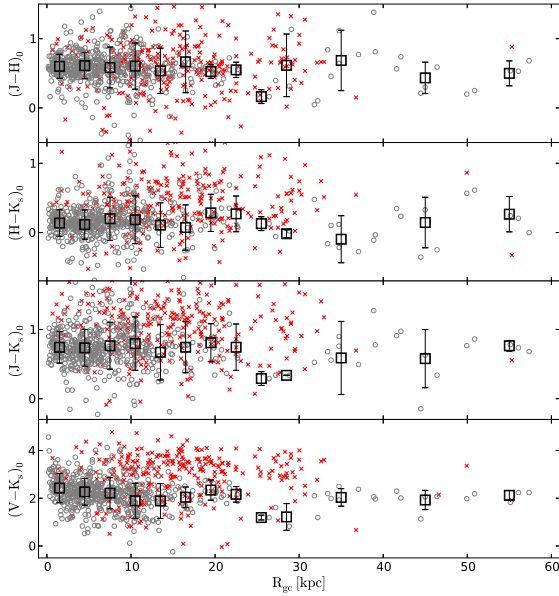


FIG. 13.— Intrinsic color as a function of galactocentric distance R_{gc} . Symbols are as in Fig. 12. The squares represent the mean color values in different projected galactocentric distance for the confirmed GCs.

The color-magnitude diagram (CMD) provides a qualitative model-independent global indication of cluster formation history (Ma 2012a, 2013). Figure 14 displays the CMD of M_K vs. $(V - K_s)_0$ for the sample star clusters with magnitude uncertainty < 0.5 mag. Symbols are as in Figure 12. The absolute magnitudes were derived with the distance modulus of $(m - M)_0 = 24.47$ with a distance of ~ 784 kpc. Several models were added to the CMD to obtain a more detailed history of cluster formation. Four fading lines from the simple stellar population (SSP) synthesis model Bruzual & Charlot (2003, hereafter BC03) for a metallicity of $Z = 0.004$, $Y = 0.24$, assuming a Salpeter (1955) stellar IMF, and using the Padova-

1994 isochrones, are plotted on the CMD of M31 star clusters for four different total initial masses: 10^6 , 10^5 , 10^4 , and $10^3 M_\odot$ (from up to bottom). It seems that many GC candidates in M31 are located out of the evolutionary tracks. The majority of M31 GCs fall between these four fading lines, consistent with previous results (Wang et al. 2010).

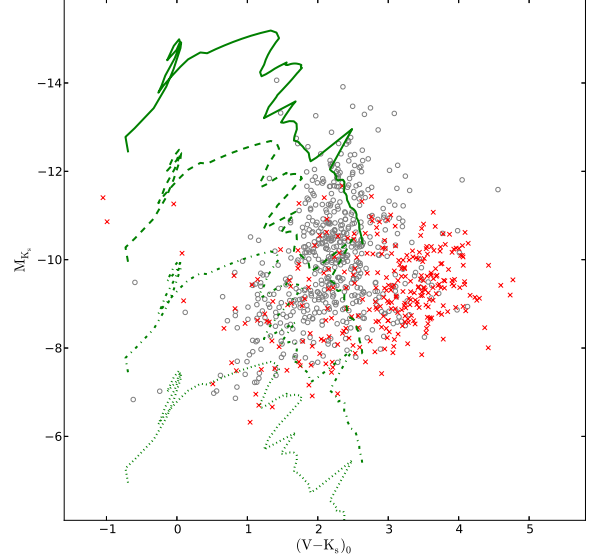


FIG. 14.— CMD of the sample clusters. Symbols are as in Fig. 12. Fading lines are indicated for clusters with total initial masses of 10^6 , 10^5 , 10^4 , $10^3 M_\odot$ (from up to bottom), assuming a Salpeter IMF.

Figure 15 shows the $(V - K_s)_0$ versus $(J - K_s)_0$ color-color diagram for M31 star clusters with magnitude uncertainty < 0.5 mag. Symbols are as in Figure 12. The theoretical evolutionary paths from the SSP model BC03 for $Z = 0.004$, $Y = 0.24$ (black line) and $Z = 0.02$, $Y = 0.28$ (green line) are displayed. The horizontal dashed line represents $V - K_s = 3$, assuming the reddening value $E(B - V) = 0.13$. As Galleti et al. (2004) reported that, most of the background galaxies have $V - K_s \geq 3$, providing a powerful tool to discriminate between M31 clusters and background galaxies. It can be seen that a large number of GC candidates are located above the dashed line, indicating that some background galaxies were mistaken for GC candidates. However, we should notice that the dashed line is just approximate to the criteria $V - K_s = 3$, since one source with $V - K_s > 3$ may be located below the dashed line if the reddening value is larger than 0.13 mag. The distribution of the clusters in the color-color diagram are much disperse, and many GC candidates are located out of the theoretical evolutionary paths, indicating that many GC candidates may not be true GCs.

4. SUMMARY

In this paper, we performed JHK_s photometric measurements for 913 GCs and candidates in the field of M31 based on 2MASS images. These sample star clusters in M31 were selected from RBC V.5, which is the latest Revised Bologna Catalog of M31 GCs and candidates. The JHK_s photometric measurements in this paper supplement this catalog, and provide a most comprehensive and homogeneous photometric

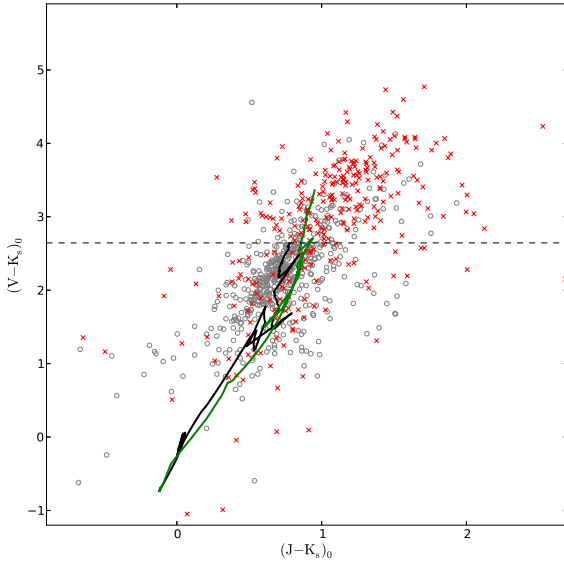


FIG. 15.— Color-color diagram of the sample clusters. Symbols are as in Fig. 12. Theoretical evolutionary paths for $Z = 0.004$, $Y = 0.24$ (black line) and $Z = 0.02$, $Y = 0.28$ (green line) are drawn. The horizontal dashed line represents $V - K_s = 3$, assuming the reddening value $E(B - V) = 0.13$.

catalog for M31 GCs in the JHK_s bandpasses. Based on detailed comparisons, our photometry is in good agreement with previous measurements. Position (right ascension and declination) for cluster H26 is corrected here (00:59:27.48 and +37:41:31.37).

We presented some statistical analysis based on the sample clusters, combined with the photometric results of 10 GCs in the M31 halo (Ma 2012b). We used least square and maximum likelihood methods to fit a Gaussian and t_5 distribution on the extinction-corrected JHK_s data. The LF peaks for all the sample clusters derived by fitting a t_5 distribution using maximum likelihood method are: $J_0 = 15.726^{+0.182}_{-0.190}$, $H_0 = 15.095^{+0.174}_{-0.182}$, and $K_{s0} = 14.816^{+0.140}_{-0.144}$ while for the confirmed GCs, the LF peaks are $J_0 = 15.348^{+0.206}_{-0.208}$, $H_0 = 14.703^{+0.176}_{-0.180}$, and $K_{s0} = 14.534^{+0.142}_{-0.146}$, which are in good agreement with

previous studies. With the division of the confirmed GCs by both galactocentric distance and metallicity, we found that the GCLFs are different between MR and MP, inner and outer subpopulations. Generally, MP clusters are fainter than their MR counterparts, and the inner clusters are brighter than the outer ones, which confirm previous results.

The NIR colors of the GC candidates are on average redder than those of the confirmed GCs, which lead to an obscure bimodal distribution of the color indices. The $(V - K_s)_0$ color index shows clearer correlation with $[Fe/H]$ than other NIR colors, indicating that those NIR intrinsic colors are less sensitive to metallicity. The relation of $(V - K_s)_0$ and metallicity shows an obvious departure from linearity, with a shallower slope towards the redder end. The CMD and color-color diagram show that many GC candidates are located out of the evolutionary tracks, indicating that some of them may not be true GCs. The CMD also shows that the initial mass of M31 clusters covers a large range, and the majority of the clusters have initial masses between 10^3 and $10^6 M_\odot$.

ACKNOWLEDGMENTS

We especially thank the anonymous referee for his/her thorough report and helpful comments and suggestions that have significantly improved the paper. This study has been supported by the Chinese National Natural Science Foundation through grants 11373035, 11373033, and 11073032, and by the National Basic Research Program of China (973 Program), No. 2014CB845702, 2014CB845704, 2013CB834902, and by the joint fund of Astronomy of the National Nature Science Foundation of China and the Chinese Academy of Science, under Grants U1231113.

This publication makes use of data products from the Two Micron All Sky Survey, which is a joint project of the University of Massachusetts and the Infrared Processing and Analysis Center/California Institute of Technology, funded by the National Aeronautics and Space Administration and the National Science Foundation.

We would like to thank the Digitized Sky Survey (DSS), which was produced at the Space Telescope Science Institute under U.S. Government grant NAG W-2166. The images of DSS are based on photographic data obtained using the Oschin Schmidt Telescope on Palomar Mountain and the UK Schmidt Telescope.

REFERENCES

- Ashman, K. M., & Bird, C. M. 1993, *AJ*, 106, 2281
 Ashman, K. M., Bird, C. M., & Zepf, S. E. 1994, *AJ*, 108, 2348
 Barmby, P., Huchra, J. P., & Brodie, J. P. 2001, *AJ*, 121, 1482
 Barmby, P., Huchra, J., Brodie, J., et al. 2000, *AJ*, 119, 727
 Barton Gillespie, E., Geller, M. J., & Kenyon, S. J. 2003, *ApJ*, 582, 668
 Baum, W. A., Hammergren, M., Groth, E. J., et al. 1995, *AJ*, 110, 2537
 Blakeslee, J. P., Cho, H., Peng, E. W., et al. 2012, *ApJ*, 746, 88
 Blakeslee, J. P., & Tonry, J. L. 1996, *ApJ*, 465, L19
 Bruzual, A. G., & Charlot, S. 2003, *MNRAS*, 344, 1000
 Caldwell, N., Harding, P., Morrison, H., et al. 2009, *AJ*, 137, 94
 Caldwell, N., Schiavon, R., Morrison, H., Rose, J. A., & Harding, P. 2011, *AJ*, 141, 61
 Cantiello, M., Blakeslee, J. P., Raimondo, G., et al. 2014, arXiv:1402.6090
 Carpenter, J. M. 2001, *AJ*, 121, 2851
 Crampton D., Cowley A. P., Schade D., & Chayer P. 1985, *ApJ*, 288, 494
 Durrell, P. R., Harris, W. E., Geisler, D., & Pudritz, R. E. 1996, *AJ*, 112, 972
 Fan, Z., de Grijs, R., & Zhou, X. 2010, *ApJ*, 725, 200
 Fan, Z., Ma, J., de Grijs, R., & Zhou, X. 2008, *MNRAS*, 385, 1973
 Ferrarese, L., Mould, J. R., Kennicutt, R. C., Jr., et al. 2000, *ApJ*, 529, 745
 Forbes, D. A., Brodie, J. P., & Huchra, J. 1997, *AJ*, 113, 887
 Galletti, S., Bellazzini, M., Buzzoni, A., Federici, L., & Fusi Pecci, F. 2009, *A&A*, 508, 1285
 Galletti, S., Federici, L., Bellazzini, M., Buzzoni, A., & Fusi Pecci, F. 2006, *A&A*, 456, 985
 Galletti, S., Federici, L., Bellazzini, M., Fusi Pecci, F., & Macrina, S. 2004, *A&A*, 426, 917
 Gebhardt, K., & Kissler-Patig, M. 1999, *AJ*, 118, 1526
 Gnedin, O. Y. 1997, *ApJ*, 487, 663
 Gordon, K. D., Bailin, J., Engelbracht, C. W., et al. 2006, *ApJ*, 638, L87
 Goudfrooij, P., Gilmore, D., Whitmore, B. C., & Schweizer, F. 2004, *ApJ*, 613, L121
 Hanes, D. A. 1977, *MNRAS*, 179, 331
 Harris, W. E. 1991, *ARA&A*, 29, 543
 Hubble, E. P. 1932, *ApJ*, 76, 44
 Huxor, A. P., Tanvir, N. R., Ferguson, A. M. N., et al. 2008, *MNRAS*, 385, 1989
 Jordán, A., McLaughlin, D. E., Côté, P., et al. 2006, *ApJ*, 651, L25
 Kang, Y., Rey, S.-C., Bianchi, L., et al. 2012, *ApJS*, 199, 37
 Kavelaars, J. J., & Hanes, D. A. 1997, *MNRAS*, 285, L31
 Kundu, A., Whitmore, B. C., Sparks, W. B., et al. 1999, *ApJ*, 513, 733
 Larsen, S. S., Brodie, J. P., Huchra, J. P., Forbes, D. A., & Grillmair, C. J. 2001, *AJ*, 121, 2974
 Ma, J. 2012a, *AJ*, 144, 41
 Ma, J. 2012b, *Research in Astronomy and Astrophysics*, 12, 115

- Ma, J. 2013, *AJ*, 145, 88
- Massey, P., Olsen, K. A. G., Hodge, P. W., et al. 2006, *AJ*, 131, 2478
- McLachlan, G. J., & Basford, K. E. 1988, *Statistics: Textbooks and Monographs*, New York: Dekker, 1988
- McLaughlin, D. E., & Pudritz, R. E. 1996, *ApJ*, 457, 578
- Miller, B. W., & Lotz, J. M. 2007, *ApJ*, 670, 1074
- Nantais, J. B., Huchra, J. P., & Barmby, P. 2006, *AJ*, 131, 1416
- Ostriker, J. P., & Gnedin, O. Y. 1997, *ApJ*, 487, 667
- Perrett, K. M., Bridges, T. J., Hanes, D. A., et al. 2002, *AJ*, 123, 2490
- Racine, R. 1968, *JRASC*, 62, 367
- Rejkuba, M. 2001, *A&A*, 369, 812
- Richardson, J. C., Ferguson, A. M. N., Mackey, A. D., et al. 2009, *MNRAS*, 396, 1842
- Salpeter, E. E. 1955, *ApJ*, 121, 161
- Santos, J. F. C., Dottori, H., & Grosbøl, P. 2013, *A&A*, 553, A74
- Secker, J. 1992, *AJ*, 104, 1472
- Secker, J., & Harris, W. E. 1993, *AJ*, 105, 1358
- Sharov, A. S. 1988, *Soviet Astronomy Letters*, 14, 339
- Skrutskie, M. F., Cutri, R. M., Stiening, R., et al. 2006, *AJ*, 131, 1163
- Skrutskie, M. F., Schneider, S. E., Stiening, R., et al. 1997, *The Impact of Large Scale Near-IR Sky Surveys*, 210, 25
- Stetson, P. B. 1987, *PASP*, 99, 191
- Strader, J., Brodie, J. P., Spitler, L., & Beasley, M. A. 2006, *AJ*, 132, 2333
- Wang, S., Fan, Z., Ma, J., de Grijs, R., & Zhou, X. 2010, *AJ*, 139, 1438
- Yoon, S.-J., Yi, S. K., & Lee, Y.-W. 2006, *Science*, 311, 1129

TABLE 1
INTEGRATED MEASUREMENTS FOR 913 CLUSTERS IN M31.

Name	J (mag)	H (mag)	K_s (mag)	r_{ap} ($''$)	$E(B-V)$ (mag)	Ref. ^a	$[Fe/H]_C$ (dex)	$[Fe/H]_K$ (dex)
(1)	(2)	(3)	(4)	(5)	(6)	(7)	(8)	(9)
AU008	15.218±0.269	14.403±0.265	14.299±0.324	4.0	0.21	5	99.99	99.99
AU010	15.440±0.211	14.665±0.230	14.504±0.251	4.0	0.22	1	-0.50	99.99
B001	14.557±0.024	13.891±0.030	13.696±0.033	7.0	0.39	1	-0.70	-0.42
B001D	17.369±0.107	17.435±0.238	17.334±0.254	4.0	0.13	6	99.99	99.99
B002	15.797±0.050	15.483±0.070	15.247±0.068	5.0	0.11	1	-2.20	99.99
B003	15.689±0.045	14.996±0.056	15.087±0.074	6.0	0.12	1	-1.60	-0.99
B004	14.966±0.030	14.371±0.034	14.136±0.034	5.0	0.18	1	-0.70	-1.00
B005	13.414±0.014	12.720±0.017	12.598±0.018	7.0	0.16	1	-0.70	-0.82
B006	13.273±0.013	12.635±0.015	12.423±0.016	12.0	0.17	1	-0.50	-0.59
B006D	17.078±0.128	16.311±0.165	15.883±0.166	4.0	0.33	1	99.99	-1.83

^aThe reddening values are from: Caldwell et al. (2009, 2011) (ref=1), Fan et al. (2008) (ref=2), Barmby et al. (2000) (ref=3), Fan et al. (2010) (ref=4), mean reddening value of clusters located within an annulus at every 2 kpc radius from the center of M31 (ref=5), and foreground reddening value of $E(B-V) = 0.13$ mag (ref=6).

TABLE 2
CLUSTERS WITH LARGE MAGNITUDE SCATTERS BETWEEN THIS PAPER AND PREVIOUS STUDIES.

Name	ΔJ (mag)	ΔH (mag)	ΔK_s (mag)	r_{ap} ($''$)
(1)	(2)	(3)	(4)	(5)
Comparison with 2MASS PSC				
B038D	-1.10			4
B072D	1.611			2
B104			-2.08	4
SK047B	-1.16			4
SK049C	-1.32			4
SK054C			-3.36	4
SK086C		1.229		4
SK115B			-1.40	4
SK136C	4.180			4
Comparison with Barmby et al. (2000, 2001)				
DAO69	1.226		1.287	4
Comparison with RBC V.5				
B017D	1.070			5
B041		1.551	1.974	3
B051D	1.411			4
B081D	1.366			5
B090			-2.60	4
B104		-1.06		4
B142D			1.077	4
B216	1.112			4
B244	1.153			5
B281D	1.153			4
B291D	1.104			4
B363	1.063			5
B452	1.264			4
B462	1.200			4
BA11	1.026			4
H7			1.164	5
M070	1.138			5
M091		-1.52		4
NB16	1.050			4
SK049C	-1.29			4
SK054C			-3.28	4
SK213B			1.118	6

TABLE 3
M31 GCLF PARAMETERS.

Bandpass	Least Square				Maximum Likelihood				N
	μ_G (mag)	σ_G (mag)	μ_t (mag)	σ_t (mag)	μ_G (mag)	σ_G (mag)	μ_t (mag)	σ_t (mag)	
(1)	(2)	(3)	(4)	(5)	(6)	(7)	(8)	(9)	(10)
All sample clusters									
J_0	15.873 ^{+0.190} _{-0.198}	1.406 ^{+0.176} _{-0.142}	15.893 ^{+0.184} _{-0.192}	1.355 ^{+0.174} _{-0.138}	15.726 ^{+0.190} _{-0.198}	1.393 ^{+0.178} _{-0.142}	15.726 ^{+0.182} _{-0.190}	1.393 ^{+0.170} _{-0.132}	914
H_0	15.224 ^{+0.178} _{-0.186}	1.340 ^{+0.170} _{-0.136}	15.245 ^{+0.174} _{-0.184}	1.290 ^{+0.168} _{-0.132}	15.095 ^{+0.178} _{-0.186}	1.377 ^{+0.170} _{-0.136}	15.095 ^{+0.174} _{-0.182}	1.377 ^{+0.166} _{-0.130}	892
K_{s0}	14.887 ^{+0.140} _{-0.144}	1.237 ^{+0.134} _{-0.108}	14.903 ^{+0.140} _{-0.146}	1.198 ^{+0.134} _{-0.106}	14.816 ^{+0.140} _{-0.144}	1.324 ^{+0.136} _{-0.108}	14.816 ^{+0.140} _{-0.144}	1.324 ^{+0.132} _{-0.104}	872
Confirmed GCs									
J_0	15.405 ^{+0.218} _{-0.222}	1.505 ^{+0.196} _{-0.160}	15.409 ^{+0.208} _{-0.212}	1.459 ^{+0.192} _{-0.148}	15.348 ^{+0.218} _{-0.220}	1.424 ^{+0.196} _{-0.158}	15.348 ^{+0.206} _{-0.208}	1.423 ^{+0.184} _{-0.144}	579
H_0	14.816 ^{+0.186} _{-0.192}	1.431 ^{+0.170} _{-0.134}	14.829 ^{+0.178} _{-0.182}	1.387 ^{+0.164} _{-0.128}	14.703 ^{+0.186} _{-0.192}	1.367 ^{+0.168} _{-0.134}	14.703 ^{+0.176} _{-0.180}	1.367 ^{+0.158} _{-0.124}	565
K_{s0}	14.621 ^{+0.144} _{-0.150}	1.354 ^{+0.136} _{-0.108}	14.640 ^{+0.142} _{-0.148}	1.310 ^{+0.134} _{-0.106}	14.534 ^{+0.144} _{-0.150}	1.357 ^{+0.136} _{-0.108}	14.534 ^{+0.142} _{-0.146}	1.357 ^{+0.132} _{-0.102}	559
Confirmed GCs (metallicity available from Kang et al.)									
J_0	14.583 ^{+0.144} _{-0.148}	1.192 ^{+0.134} _{-0.110}	14.596 ^{+0.140} _{-0.144}	1.141 ^{+0.132} _{-0.108}	14.534 ^{+0.146} _{-0.146}	1.180 ^{+0.134} _{-0.110}	14.534 ^{+0.138} _{-0.144}	1.180 ^{+0.130} _{-0.104}	287
H_0	14.031 ^{+0.130} _{-0.132}	1.214 ^{+0.120} _{-0.098}	14.051 ^{+0.126} _{-0.130}	1.162 ^{+0.122} _{-0.096}	13.982 ^{+0.130} _{-0.134}	1.221 ^{+0.122} _{-0.098}	13.982 ^{+0.126} _{-0.130}	1.214 ^{+0.120} _{-0.094}	287
K_{s0}	13.902 ^{+0.098} _{-0.100}	1.214 ^{+0.088} _{-0.074}	13.927 ^{+0.096} _{-0.098}	1.150 ^{+0.090} _{-0.076}	13.862 ^{+0.098} _{-0.100}	1.225 ^{+0.088} _{-0.074}	13.861 ^{+0.094} _{-0.098}	1.161 ^{+0.088} _{-0.074}	288

TABLE 4
M31 GCLF PARAMETERS FOR FOUR GROUPS OF THE CONFIRMED GCs.

Subsample	J_0			H_0			K_{s0}		
	μ_t (mag)	σ_t (mag)	N	μ_t (mag)	σ_t (mag)	N	μ_t (mag)	σ_t (mag)	N
(1)	(2)	(3)	(4)	(5)	(6)	(7)	(8)	(9)	(10)
MR inner	14.140 ^{+0.118} _{-0.120}	1.157 ^{+0.104} _{-0.084}	139	13.548 ^{+0.096} _{-0.098}	1.171 ^{+0.084} _{-0.070}	139	13.400 ^{+0.106} _{-0.110}	1.130 ^{+0.092} _{-0.076}	139
MP inner	14.904 ^{+0.064} _{-0.064}	1.067 ^{+0.064} _{-0.054}	83	14.413 ^{+0.062} _{-0.064}	1.123 ^{+0.066} _{-0.056}	84	14.294 ^{+0.050} _{-0.050}	1.022 ^{+0.048} _{-0.044}	84
MR outer	14.672 ^{+0.044} _{-0.044}	0.874 ^{+0.036} _{-0.032}	25	14.118 ^{+0.064} _{-0.062}	0.980 ^{+0.050} _{-0.042}	25	13.910 ^{+0.064} _{-0.066}	0.996 ^{+0.054} _{-0.046}	25
MR outer	15.033 ^{+0.084} _{-0.080}	1.079 ^{+0.068} _{-0.058}	43	14.484 ^{+0.052} _{-0.052}	1.041 ^{+0.042} _{-0.036}	42	14.430 ^{+0.046} _{-0.044}	1.009 ^{+0.038} _{-0.034}	43

TABLE 5
RESULTS FROM THE KMM HOMOSCEDASTIC BIMODALITY TESTS FOR THE JHK_s COLORS OF THE SAMPLE CLUSTERS IN M31.

Data set	Δ (mag)	σ_Δ (mag)	Δ_1 (mag)	Δ_2 (mag)	σ_Δ (mag)	N_1	N_2	p
(1)	(2)	(3)	(4)	(5)	(6)	(7)	(8)	(9)
$(J - H)_0$	0.600	0.101	0.579	1.573	0.080	840	16	0.000
$(H - K_s)_0$	0.240	0.114	0.193	0.979	0.079	779	38	0.000
$(J - K_s)_0$	0.845	0.155	0.801	1.622	0.120	812	29	0.000
$(V - K_s)_0$	2.423	0.696	2.324	2.560	0.683	718	125	...

TABLE 6
RESULTS FROM THE KMM HOMOSCEDASTIC BIMODALITY TESTS FOR THE METALLICITIES OF THE SAMPLE CLUSTERS IN M31.

Data set	[Fe/H] (dex)	$\sigma_{[\text{Fe}/\text{H}]}$ (dex)	[Fe/H] ₁ (dex)	[Fe/H] ₂ (dex)	$\sigma_{[\text{Fe}/\text{H}]}$ (dex)	N_1	N_2	p
(1)	(2)	(3)	(4)	(5)	(6)	(7)	(8)	(9)
Caldwell et al.	-1.010	0.345	-0.934	-1.772	0.287	303	9	0.361
Kang et al.	-1.032	0.350	-0.632	-1.527	0.152	167	127	0.002

APPENDIX

SEVERAL SANITY CHECKS OF THE 2MASS PHOTOMETRY

This appendix addresses the need to clarify the procedure adopted to obtain the best measurement of the aperture photometry of each GC candidate. Two checks of the 2MASS photometry were given as follows.

A test of the photometry comparing results from the 2MASS-6X and the 2MASS All-Sky images was performed, considering that objects with low S/N may have underestimated magnitudes being near the magnitude limits of the 2MASS All-Sky images. This test may shed some light on the amount of photons lost for faint objects and provide the safest magnitude limits at which to stop the analysis. Figure 1 displays the photometry comparison of the same objects in both 2MASS-6X and 2MASS All-sky images, with same photometry methods. However, no clear trend can be seen that photons are lost for faint objects. In this paper, no magnitude limits were set to stop the statistical analysis.

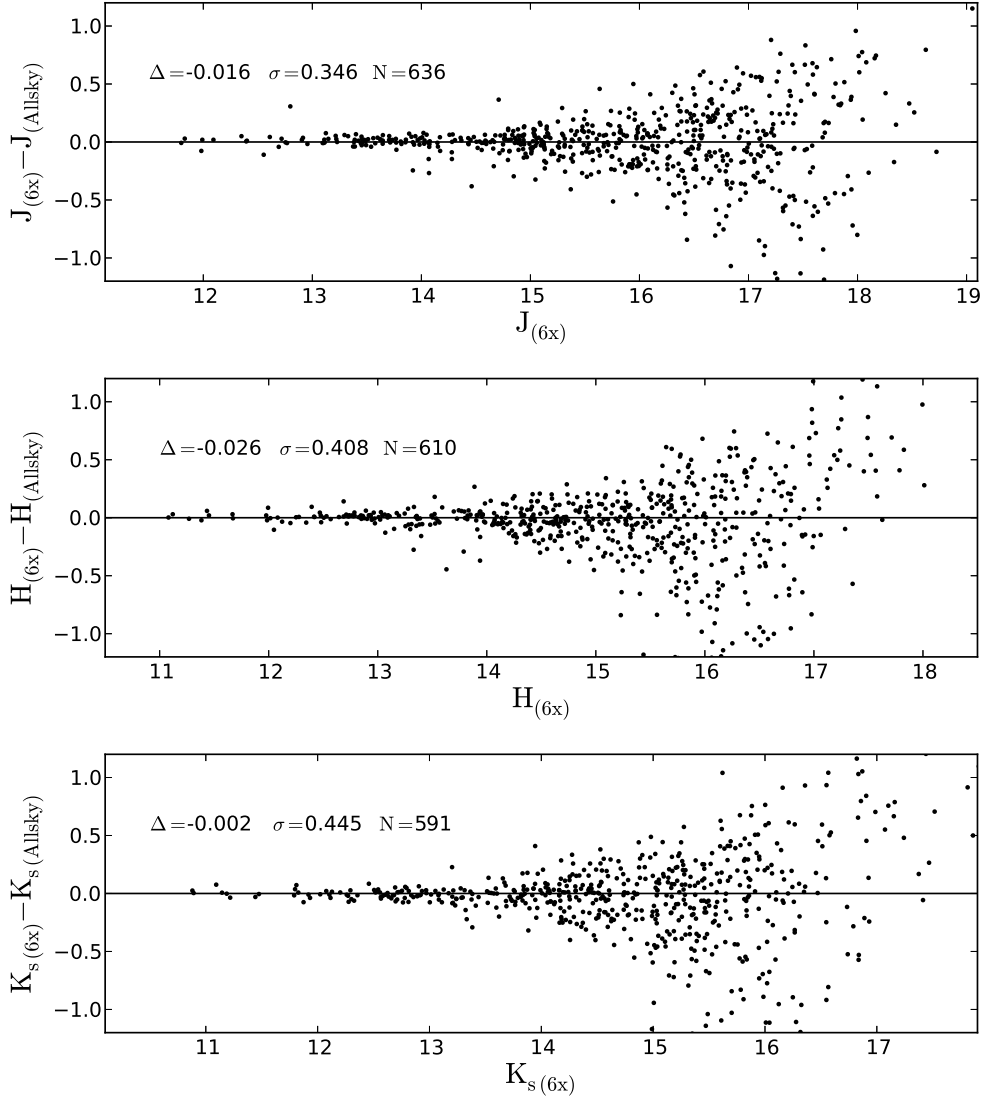


FIG. 1.— Comparison of the obtained photometry from the 2MASS-6X and the 2MASS All-sky images.

As was mentioned in section 2.2, we chose the annulus, which is the “dannulus” in DAOPHOT, of 5 pixels following our experience. A test about the effect of annulus on photometry was performed, with annulus ranging from 5 pixels to 9 pixels. Figure 2 shows the comparison of J -band magnitudes with different set of annulus. No significant trend can be seen. We think that the annulus set in this paper is reasonable and could assure a proper estimate of the sky.

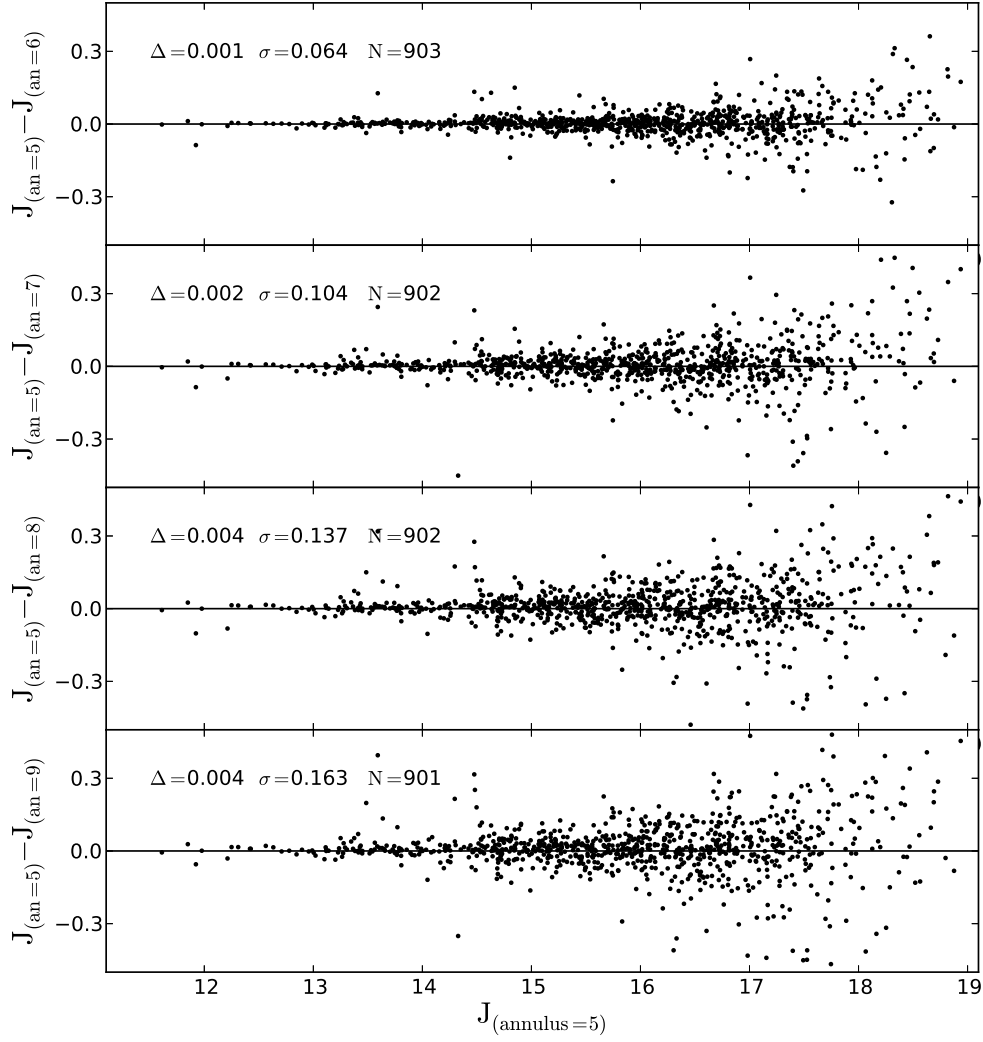


FIG. 2.— Comparison of the obtained J -band photometry with different set of annulus.